The Astrophysical Journal Letters, 901:L23 (5pp), 2020 October 1 https://doi.org/10.3847/2041-8213/abb81e

The Downwind Solar Wind: Model Comparison with Pioneer 10 Observations

M. Nakanotani[1], G. P. Zank[1,2], L. Adhikari[1], L.-L. Zhao[1], J. Giacalone[3], M. Opher[4], and J. D. Richardson[5]
[1] Center for Space Plasma and Aeronomic Research (CSPAR), University of Alabama in Huntsville, Huntsville, AL 35805, USA; mn0052@uah.edu
[2] Department of Space Science, University of Alabama in Huntsville, Huntsville, AL 35899, USA
[3] Lunar & Planetary Laboratory, University of Arizona, Tucson, AZ 85721, USA
[4] Astronomy Department, Boston University, Boston, MA 02215, USA
[5] Kavli Institute for Astrophysics and Space Research and Department of Physics, Massachusetts Institute of Technology, Cambridge, MA 02139, USA
Received 2020 August 29; revised 2020 September 7; accepted 2020 September 10; published 2020 September 25

Abstract

The solar wind in the upwind region has been well modeled using a pickup ion (PUI) mediated MHD model (Zank et al.). It suggests that PUIs have an important role in heating the solar wind in the outer heliosphere. However, the solar wind in the downwind region is not as well understood. Here, we compare the Zank et al. model with Pioneer 10 observations, which allows us to investigate the downwind solar wind out to 60 au. We use a model in which the hydrogen temperature is finite to obtain a proper hydrogen number density distribution in the downwind region and incorporate it into the model. Our results explain Pioneer 10 observations well and indicate that the heating due to PUIs is less effective than in the upwind region since the density of PUIs in the downwind region is less than the upwind PUIs density. We also derive parameters at several possible locations of the downwind termination shock.

Unified Astronomy Thesaurus concepts: Solar wind (1534); Solar physics (1476); Magnetohydrodynamics (1964); Pickup ions (1239)

1. Introduction

The solar wind is greatly modified by interstellar neutral atoms (mainly hydrogen; Zank 1999, 2015, and references therein). The interstellar medium comprises plasma and neutral atoms, and the latter enters the heliosphere with speeds of $\sim$26 km s^{-1} (helium) and $\sim$20 km s^{-1} (hydrogen) in the Sun's rest frame (Witte 2004; McComas et al. 2012; Zank et al. 2013). While the interstellar plasma interacts with the solar wind plasma and the interaction produces several boundaries, such as the termination shock, the heliopause, and a bow shock/wave, interstellar neutral atoms enter the heliosphere because they do not react to any electromagnetic fields and are weakly coupled to the charged particles. Neutral atoms entering the solar wind experience charge exchange and form a ring beam about the mean magnetic field and are called pickup ions (PUIs). The newly born PUIs are unstable and excite waves (Lee & Ip 1987; Williams & Zank 1994; Hellinger & Trávníček 2016; Smith et al. 2017; Hollick et al. 2018a, 2018b), which contribute to heating the ambient solar wind plasma (Matthaeus et al. 1999; Smith et al. 2007; Adhikari et al. 2015, 2017; Zank et al. 2017).

The modification of the solar wind due to hydrogen PUIs has been modeled and well explains Voyager 2 and New Horizons Solar Wind Around Pluto observations (Zank et al. 2018; Zhao et al. 2019). The Zank et al. (2018) model couples mean solar wind variables and PUIs with turbulence transport equations (Adhikari et al. 2017; Zank et al. 2017) that include turbulence heating terms related to PUIs and shear flows. The effect of the PUI turbulence heating is evident after 30 au in both the model and Voyager 2 plasma observations in the upwind region. The upwind direction is defined as the direction antiparallel to the incident interstellar medium. In the absence of PUIs, the thermal temperature in the distant solar wind is much less than predicted by a PUI-mediated model.[6] Therefore, it is crucial to consider the inclusion of PUIs.

The solar wind in the downwind direction has not been investigated extensively. The downwind direction is defined as the direction parallel to the incident interstellar medium flow. A primary difference between the upwind and downwind solar wind may come from differences in the upwind and downwind hydrogen (H) number density distributions. The H number density distribution in the downwind region is highly variable and in particular depends on solar activity. The H number density can be lower downwind than in the upwind region, when the solar radiation pressure exceeds the gravitational attraction on H atoms. Therefore, in this case, it might be expected that the downwind solar wind is less affected by PUIs than the upwind. Some observations by Pioneer 10 suggest that PUIs may have been observed in the downwind region (Intriligator et al. 1996; Mihalov & Gazis 1998).

In this Letter, we compare our model of a PUI-mediated solar wind with Pioneer 10 observations. Pioneer 10 gives us an opportunity to investigate the solar wind in the downwind region of the outer heliosphere out to 60 au. In the next section, we specify the H number density distribution in the downwind region that we incorporate into our model. Section 3 provides a comparison of our model with Pioneer 10 observations.

[6] One-fluid plasma models that incorporate PUIs and thermal plasma indistinguishably (e.g., Holzer 1972; Khabibrakhmanov et al. 1996; Zank 1999) including global models (Pauls et al. 1995; Zank et al. 1996, 2013; Zank 1999; Pogorelov et al. 2017; Washimi et al. 2017) exhibit an increase in the apparent temperature of the solar wind, by several orders of magnitude. This is of course not observed and reflects only that suprathermal PUIs and cooler thermal solar wind plasma have been co-mingled. A discussed in Isenberg (1987) and Zank et al. (2014), PUIs and thermal solar wind protons do not equilibrate and should be considered separately if one addresses the thermodynamics of the solar wind. PUIs heat the solar wind indirectly, by exciting turbulence in the outer heliosphere. The subsequent dissipation of turbulence results in the heating of the solar wind. This is in the approach developed by Zank et al. (2018) and followed here.

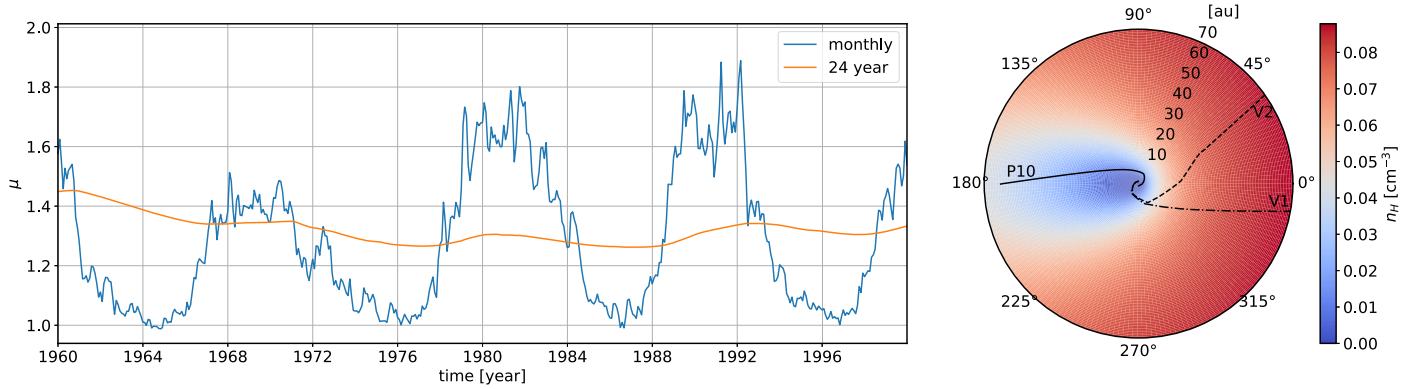

Figure 1. Left panel: monthly (blue) and 24 yr (orange) average of the ratio μ of solar radiation pressure to solar gravity; right panel: hydrogen density distribution and the trajectories of Pioneer 10 and Voyager 1 and 2. The H distribution is based on the "hot model" (Wu & Judge 1979; Thomas 1978).

Finally, we summarize our results and discuss some possible properties of the downwind termination shock and its potential relationship with energetic neutral atoms (ENAs).

2. Hydrogen Number Density Distribution in the Heliosphere

To model the solar wind properly, we need to know the distribution of neutral atoms inside the heliosphere. Here, we only consider hydrogen since it is the dominant neutral component of the heliosphere. The H number density in the heliosphere can be derived from the ballistic propagation of a hydrogen atom experiencing the forces of both solar gravity and Lyman-α (Lyα) radiation pressure. Here we assume that the solar Lyα radiation pressure is spherically symmetric (we ignore the Poynting–Robertson effect since $u_H/c \ll 1$ where u_H and c are the hydrogen bulk flow speed and the speed of light, respectively).

The ratio μ of solar radiation pressure to solar gravity determines distribution of hydrogen in the heliosphere. When $\mu < 1$, hydrogen tends to be focused in the downwind region. On the other hand, when $\mu > 1$, hydrogen tends to be excluded from the downwind region. The left panel of Figure 1 shows monthly (blue) and 24 yr (orange) averaged variation of μ from 1960 to 2000. We use the new Version 4 solar Lyman-α composite data set[7] (Machol et al. 2019) and calculate μ according to Bzowski et al. (2008). The factor μ varies with solar activity and the peaks correspond to solar maximum and μ ranges from 1 to 2. Since the ratio μ is almost constant around 1.3 in the 24 yr averaged one, we take $\mu = 1.3$ for our model and assume that the H distribution in our model is time independent. Note that an interstellar H atom takes ~24 yr to reach ~100 au in the downwind direction assuming a speed ~20 km s^{-1}.

Here, we adopt the "hot model" (Thomas 1978; Wu & Judge 1979) to calculate the density distribution for which a finite hydrogen temperature is considered. We assume that interstellar hydrogen enters the heliosphere with parameters $n_H = 0.1$ cm^{-3}, bulk flow speed $u_H = 20$ km s^{-1}, and temperature $T_H = 6500$ K (Zank et al. 2013, 2018). The right panel of Figure 1 shows the number density distribution of hydrogen. We superimpose the Pioneer 10 and Voyager 1 and 2 trajectories. Pioneer 10 traveled in the downwind region where the H number density is low, whereas Voyager 1 and 2 traveled in the upwind region where the H number density is high. We take a cut along the heliospheric axis defined by $\theta = 175°$, which provides a reference density distribution that is incorporated into our model. This distribution is well approximated by $\exp(-L\theta/r \sin\theta)$ where r is the heliospheric distance and $L = 2$ au. We confirmed that the H number density when $\mu = 1.1$ and 1.6 as a function of the heliocentric distance for $\theta = 175°$ are ~1.2 and ~0.8 times the H number density of $\mu = 1.3$ for a distance greater than 40 au. This indicates that our assumption of using a constant $\mu = 1.3$ is reasonable. We note that the H number density distribution in the upwind region is also well approximated by the same function but with $\theta = 0°$ and $L = 7$ au.

3. Model and Observations

Our model is comprised of the nearly incompressible turbulence transport equations (Zank et al. 2017; Adhikari et al. 2017) that are coupled to the background solar wind variables including PUIs (Zank et al. 2018). Note that the model is an energy-containing model that assumes a Kolmogorov phenomenology to describe the inertial range of solar wind turbulence. Specifically, we solve the time-dependent and spherically symmetric form of Equations (14)–(17), (19)–(21), and (22)–(31) in Zank et al. (2018) using the cubic interpolated profile (CIP) scheme (Yabe et al. 1991; Kudoh & Shibata 1997). Here, we consider PUIs and shear flows as the driving turbulence, which is then dissipated and heats the thermal plasma. The H number density distribution discussed above is necessary to evaluate the PUI creation rate and hence the rate at which turbulence is generated in the outer heliosphere.

The boundary conditions at 1 au and model parameters are listed in Tables 1 and 2, respectively. We use the same boundary conditions except for the PUI parameters and slightly modified model parameters used in Zank et al. (2018) for Voyager 2 observations. Note that Pioneer 10 and Voyager 2 observations overlap with each other and the difference in the heliospheric distance of each spacecraft was about 10 au. Using the same boundary conditions is useful to clarify the difference between the downwind and upwind solar wind.

Figure 2 shows a comparison of the mean solar wind variables modeled (red line) and observed by Pioneer 10 (filled points). The black dashed line corresponds to the mean variables of the upwind solar wind obtained from the same model but with $u_H = 20$ km s^{-1}, $\theta = 0°$, and $L = 7$ au. The top left panel shows the magnitude of the azimuthal magnetic

[7] http://lasp.colorado.edu/lisird/data/composite_lyman_alpha/

Table 1
Boundary Values at 1 au for the Mean Plasma and Magnetic Field and Turbulence Variables

Mean		2D Core Turbulence		Slab Turbulence	
U	440 km s^{-1}	$\langle z^{\infty+2}\rangle$	1600 km^2 s^{-2}	$\langle z^{*+2}\rangle$	400 km^2 s^{-2}
n_s	7 cm^{-3}	$\langle z^{\infty-2}\rangle$	160 km^2 s^{-2}	$\langle z^{*-2}\rangle$	40 km^2 s^{-2}
n_p	1.55×10^{-36} cm^{-3}	E_D^{∞}	-80 km^2 s^{-2}	E_D^{*}	-20 km^2 s^{-2}
P_s	1×10^{-11} Pa	L_{∞}^{+}	2.95×10^9 km^3 s^{-2}	L_{*}^{+}	2.95×10^8 km^3 s^{-2}
P_p	1.4×10^{-46} Pa	L_{∞}^{-}	2.65×10^8 km^3 s^{-2}	L_{*}^{-}	1.66×10^8 km^3 s^{-2}
B	5 nT	L_D^{∞}	-1.7×10^8 km^3 s^{-2}	L_D^{*}	-4.22×10^7 km^3 s^{-2}

Table 2
Model Parameters that Enter Equations (14)–(17), (19)–(21), and (22)–(32) in Zank et al. (2018)

Parameters	Values	Parameters	Values
b	0.22	ν_{p0}	1.5×10^{-7} s^{-1}
C_{sh}^{+}	2.5	τ_{ion}^{0}	10^6 s
C_{sh}^{-}	2.5	n_{sw}^{0}	7 cm^{-3}
$C_{sh}^{E_D}$	-1	n_H^{∞}	0.1 cm^{-3}
C_{sh}^{*+}	1.5	u_H	-20 km s^{-1}
C_{sh}^{*-}	1.5	T_H	6500 K
$C_{sh}^{*E_D}$	-0.5	α	0.2
f_D	0.18	ν_{c0}	2×10^{-15} cm^{-2}
ΔU	200 km s^{-1}	V_{A0}	40 km s^{-1}

field, the top right panel the bulk solar wind flow speed, the bottom left panel the thermal solar wind plasma and PUI number density, and the bottom right panel the thermal plasma and PUI temperature. We use Pioneer 10 1 hr resolution data and average the data following Zank et al. (1996) and Adhikari et al. (2014) except that we allow for at least two (rather than five) points in a 10 hr sliding window. Overall, our model demonstrates good agreement with the observations. The magnetic field data are lacking after 8 au, and the model and the data are slightly different. They may become consistent as the heliospheric distance increases. Several disturbances that were seen in the flow speed observations are not considered in our model. The thermal plasma density follows the well-known radial heliocentric dependence, $n_s \propto r^{-2}$. According to our model the downwind PUI number density is considerably lower within 10 au compared to the upwind region (the black dashed line), and continues to increase, whereas a peak is observed at $\sim$12 au in the upwind region. We see that the upwind and downwind theoretical temperature curves are the same up to about 15 au and both are consistent with the data up to that distance. Thereafter, the upwind solution flattens and then slowly increases, diverging from the observed downwind temperature, which is due to the dissipation of PUI-driven turbulence and becomes noticeable beyond $\sim$30 au (the black dashed line), as seen in Voyager 2 observations. The downwind solution continues to track the observations well up to about 60 au, after which the data regrettably end, and the predicted downwind temperature begins to slowly increase due to the dissipation of PUI-excited waves. This is unfortunate because the temperature data hint that they too may be flattening at that point. Our model captures this profile well and predicts furthermore that PUI-driven turbulence heating becomes significant after 60 au. The PUI temperature profile in our model stays almost constant. It is also seen in our model that the deceleration of the flow occurs after 50 au in response to the increased thermal pressure. PUI heating in the downwind region is less efficient than that in the upwind region simply because the H number density in the downwind region is less than that in the upwind region. We conclude that using a proper hydrogen density distribution is crucial in determining the solar wind profile in the downwind region and our model suggests that PUIs may mediate the downwind region less efficiently than in the upwind region but this needs to be considered further, particularly it in the context of global models (Washimi et al. 2017).

4. Summary and Discussions

We have shown that our model explains well the downwind solar wind profiles observed by Pioneer 10. A ratio $\mu = 1.3$, which controls the hydrogen density distribution in the heliosphere was derived from the Lyα observations for the period that Pioneer 10 was making measurements. We use the "hot model" for hydrogen to properly estimate the hydrogen density distribution in the downwind region. We solved a model that couples turbulence transport equations with the background solar wind and PUIs and compared with Pioneer 10 observations. Our model fits the observations well and indicates that PUI turbulence heating occurs after 50 au. The temperature profile observed by Pioneer 10 does not show any apparent heating due to PUIs. The distance at which PUI-driven turbulence heating occurs is predicted to be larger than the distance observed in the upwind region. The reason is simply because the hydrogen density in the downwind region is lower than that upwind and the driving of PUI turbulence and hence dissipative heating is not efficient before 60 au. Unlike Zank et al. (2018), we do not present the model turbulence properties since the lack of magnetic field data prevents a comparison.

Our model enables us to estimate upstream plasma, PUI, and turbulence values at the downwind termination shock. Since the downwind termination shock has not been observed, we choose 100, 150, and 200 au as possible distances to the termination shock. These distances are roughly consistent with locations observed in MHD simulations (Zank & Müller 2003; Izmodenov et al. 2005; Pogorelov et al. 2017; Washimi et al. 2017; Opher et al. 2020). These parameters are listed in Table 3, and we also include upstream parameters for the upwind termination shock for comparison. We derive the PUI to thermal plasma density ratio, Alfvén Mach number, fast magnetosonic Mach number including the PUI pressure, and the PUI to thermal pressure ratio from the model values. The fast magnetosonic Mach number is also an important parameter to determine the structure of a PUI-mediated shock wave (Zieger et al. 2015). Overall, the PUI pressure dominates the

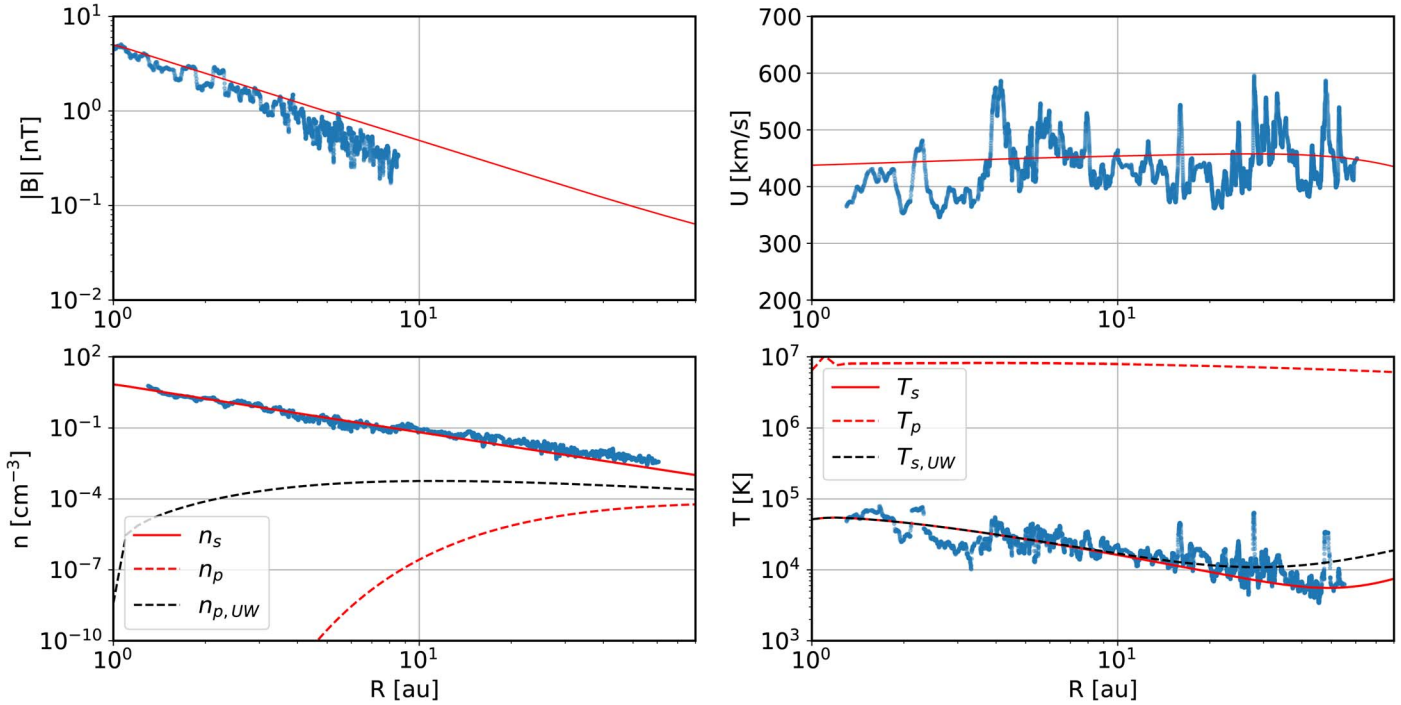

Figure 2. The theoretical model for the downwind solar wind (red line), and Pioneer 10 observations (filled points). Top left: the magnitude of the background azimuthal magnetic field, top right: the bulk flow speed, bottom left: the thermal plasma (solid) and PUI (dashed) number density, and bottom right: the thermal plasma (solid) and PUI (dashed) temperature. Black dashed line is the upwind solar wind obtained from the same model but with $u_H = 20\,\mathrm{km\,s^{-1}}$, $\theta = 0°$, and $L = 7$ au.

Table 3
Upstream Values of the Termination Shock in the Upwind (UW) Region at 84 au and the Downwind (DW) Region at 100, 150, and 200 au

	UW_{84}	DW_{100}	DW_{150}	DW_{200}
n_s (cm^{-3})	9.34×10^{-4}	6.63×10^{-4}	3.02×10^{-4}	1.77×10^{-4}
n_p (cm^{-3})	2.39×10^{-4}	0.633×10^{-4}	0.676×10^{-4}	0.695×10^{-4}
U (km s^{-1})	369	420	373	323
B (nT)	0.07	0.05	0.04	0.034
T_s (K)	1.98×10^4	1.01×10^4	1.94×10^4	3.18×10^4
T_p (K)	351×10^4	588×10^4	531×10^4	480×10^4
$\frac{n_p}{n_s+n_p} \times 100$ (%)	20	8.7	18	28
M_A	7.38	9.5	7.46	5.77
M_{ms}	2.07	1.87	1.73	1.55
P_p/P_s	22.7	27.8	30.6	29.6

Note. The values in the upwind region at 84 au are calculated with the same boundary conditions and model parameters but with $u_H = 20\,\mathrm{km\,s^{-1}}$, $\theta = 0°$, and $L = 7$ au.

thermal plasma pressure for each location, and the ratios of the downwind termination shock are larger than those of the upwind termination shock. At 100 au in the downwind region, the density ratio and the Mach number are smaller and larger than those at 84 au in the upwind region, respectively. The downwind termination shock at 150 au is likely to be similar to the upwind termination shock since the parameters are close to those at 84 au in the upwind region. The nondimensional parameters suggest that a downwind termination shock at 200 au would be weak and greatly modified by PUIs since the density ratio is large (=28%) and $M_A = 5.77$. The location and the upstream values of the termination shock in the downwind region are critical to determine the properties of PUIs and thermal protons downstream of the heliospheric termination shock (Zank et al. 1996, 2010). This in turn determines the ENA flux emanating from the inner heliosheath (Zank et al. 2010; Desai et al. 2012, 2013; Heerikhuisen et al. 2014; Zirnstein et al. 2016).

We acknowledge the partial support of an NSF EPSCoR RII-Track-1 Cooperative Agreement OIA-1655280, an NSF/DOE Partnership in Basic Plasma Science and Engineering via NSF grant PHY-1707247, and a NASA grant 18-DRIVE18_2-0029, Our Heliospheric Shield, 80NSSC20K0603. We also acknowledge use of NASA/GSFC's Space Physics Data Facility's CDAWeb to obtain data.

ORCID iDs

M. Nakanotani https://orcid.org/0000-0002-7203-0730
G. P. Zank https://orcid.org/0000-0002-4642-6192
L. Adhikari https://orcid.org/0000-0003-1549-5256
L.-L. Zhao https://orcid.org/0000-0002-4299-0490
M. Opher https://orcid.org/0000-0002-8767-8273
J. D. Richardson https://orcid.org/0000-0003-4041-7540

References

Adhikari, L., Zank, G. P., Bruno, R., et al. 2015, ApJ, 805, 63
Adhikari, L., Zank, G. P., Hu, Q., & Dosch, A. 2014, ApJ, 793, 52
Adhikari, L., Zank, G. P., Hunana, P., et al. 2017, ApJ, 841, 85
Bzowski, M., Möbius, E., Tarnopolski, S., Izmodenov, V., & Gloeckler, G. 2008, A&A, 491, 7
Desai, M. I., Allegrini, F. A., Bzowski, M., et al. 2013, ApJ, 780, 98
Desai, M. I., Allegrini, F. A., Dayeh, M. A., et al. 2012, ApJL, 749, L30
Heerikhuisen, J., Zirnstein, E. J., Funsten, H. O., Pogorelov, N. V., & Zank, G. P. 2014, ApJ, 784, 73
Hellinger, P., & Trávníček, P. M. 2016, ApJ, 832, 32
Hollick, S. J., Smith, C. W., Pine, Z. B., et al. 2018a, ApJ, 863, 75
Hollick, S. J., Smith, C. W., Pine, Z. B., et al. 2018b, ApJ, 863, 76
Holzer, T. E. 1972, JGR, 77, 5407
Intriligator, D. S., Siscoe, G. L., & Miller, W. D. 1996, GeoRL, 23, 2181
Isenberg, P. A. 1987, JGR, 92, 1067
Izmodenov, V., Malama, Y., & Ruderman, M. S. 2005, A&A, 429, 1069
Khabibrakhmanov, I. K., Summers, D., Zank, G. P., & Pauls, H. L. 1996, ApJ, 469, 921
Kudoh, T., & Shibata, K. 1997, ApJ, 476, 632
Lee, M. A., & Ip, W. H. 1987, JGR, 92, 11041
Machol, J., Snow, M., Woodraska, D., et al. 2019, E&SS, 6, 2263
Matthaeus, W. H., Zank, G. P., Smith, C. W., & Oughton, S. 1999, PhRvL, 82, 3444
McComas, D. J., Alexashov, D., Bzowski, M., et al. 2012, Sci, 336, 1291
Mihalov, J. D., & Gazis, P. R. 1998, GeoRL, 25, 241
Opher, M., Loeb, A., Drake, J., & Toth, G. 2020, NatAs, 4, 675
Pauls, H. L., Zank, G. P., & Williams, L. L. 1995, JGR, 100, 21595
Pogorelov, N. V., Heerikhuisen, J., Roytershteyn, V., et al. 2017, ApJ, 845, 9
Smith, C. W., Aggarwal, P., Argall, M. R., et al. 2017, JPhCS, 900, 012018
Smith, C. W., Vasquez, B. J., Hamilton, K., et al. 2007, in AIP Conf. Proc. 932, Turbulence and Nonlinear Processes in Astrophysical Plasmas (Melville, NY: AIP), 96
Thomas, G. E. 1978, AREPS, 6, 173
Washimi, H., Tanaka, T., & Zank, G. P. 2017, ApJL, 846, L9
Williams, L. L., & Zank, G. P. 1994, JGR, 99, 19229
Witte, M. 2004, A&A, 426, 835
Wu, F. M., & Judge, D. L. 1979, ApJ, 231, 594
Yabe, T., Ishikawa, T., Wang, P. Y., et al. 1991, CoPhC, 66, 233
Zank, G. P. 1999, SSRv, 89, 413
Zank, G. P. 2015, ARA&A, 53, 449
Zank, G. P., Adhikari, L., Zhao, L. L., et al. 2018, ApJ, 869, 23
Zank, G. P., Du, S., & Hunana, P. 2017, ApJ, 842, 114
Zank, G. P., Heerikhuisen, J., Pogorelov, N. V., Burrows, R., & McComas, D. 2010, ApJ, 708, 1092
Zank, G. P., Heerikhuisen, J., Wood, B. E., et al. 2013, ApJ, 763, 20
Zank, G. P., Hunana, P., Mostafavi, P., & Goldstein, M. L. 2014, ApJ, 797, 87
Zank, G. P., Matthaeus, W. H., & Smith, C. W. 1996, JGR, 101, 17093
Zank, G. P., & Müller, H. R. 2003, JGRA, 108, 1240
Zank, G. P., Pauls, H. L., Williams, L. L., & Hall, D. T. 1996, JGR, 101, 21639
Zhao, L.-L., Zank, G. P., & Adhikari, L. 2019, ApJ, 879, 32
Zieger, B., Opher, M., Tóth, G., Decker, R. B., & Richardson, J. D. 2015, JGRA, 120, 7130
Zirnstein, E. J., Funsten, H. O., Heerikhuisen, J., et al. 2016, ApJ, 826, 58